NTNU
Norwegian University of
Science and Technology

A New Method for Aliasing Correction in Vector Doppler Ultrasound: Evaluation of a Duplex Setup

Thesis for the degree of Master
Trondheim, June 2019

Manar Alsenwar

DEPARTMENT OF ELECTRONIC SYSTEMS
NORWEGIAN UNIVERSITY OF SCIENCE AND TECHNOLOGY

Summary

Doppler ultrasound is a very useful tool in clinical practice, and is used for blood velocity estimation. However, all flow velocity estimates are one-dimensional, resulting in estimates that are dependent on the flow angle. Vector Doppler imaging is a proposed method in this context, as it provides this angle-dependency. However, the vector Doppler modality suffers from one fundamental challenge, which is aliasing of velocity estimates.

In this work, a duplex acquisition and processing setup was proposed producing high quality B-mode images with overlaid vector Doppler velocity estimates with aliasing correction. The aliasing correction method was first optimized using simulations. The method was then assessed using ultrasound recordings from a flow phantom, and *in vivo* recordings from a human carotid artery. The results indicate that the method is relatively robust when using a Doppler packet size of 150. Lower robustness of the method was observed when the flow signal contained high variance, due to very high velocities or accelerated flow. However, the results showed that the method is robust to low SNR.

Contents

Abbreviations

B-mode	Brightness mode
CDI	Color Doppler imaging
CFI	Color flow imaging
CT	Computed tomography
CVD	Cardiovascular disease
CW-Doppler	Continuous wave Doppler
$f_{\#}$	F-number
FIR	Finite impulse response
FWHM	Full width half maximum
IIR	Infinite impulse response
IQ	In-phase Quadrature
MRI	Magnetic resonance imaging
PRF	Pulse repetition frequency
PRT	Pulse repetition time
PW-Doppler	Pulsed wave Doppler
RF	Radio frequency
ROI	Region of interest
Rx	receive
SNR	Signal-to-noise ratio
$\mathrm{T}_{\mathrm{PRF}}$	1/PRF = PRT
Tx	transmit

Chapter 1

Introduction

According to the World Health Organization (WHO), cardiovascular disease is the main cause of death globally [1]. Cardiovascular disease occurs due to disorders of the conditions of blood vessels, and typically leads to either occlusion or narrowing of the blood vessels. Hence, early detection and prevention of cardiovascular disease has become a main subject of interest in clinical practice.

Ultrasound imaging is today the primary imaging modality used to examine patients with cardiovascular disease symptoms. Although several other imaging modalities, such as CT and MRI, are currently used to detect blocked arteries, the ability to measure blood velocities is important to detect narrowings and occlusions. Ultrasound is a suitable tool in this context as it has the ability to measure blood velocities in real-time. Other advantages of ultrasound imaging is that it does not use ionizing radiation, and that it is cheaper and more accessible compared with other modalities. In addition, most ultrasound imaging applications are non-invasive as they do not require the use of contrast.

Ultrasound imaging of moving objects within the body including blood is commonly referred to as Doppler ultrasound. The Doppler modality is based on detecting the change in frequency or phase that occurs when the transmitted ultrasound wave is scattered by moving blood scatterers. By measuring this frequency or phase shift, blood velocities may be estimated noninvasively.

Today, there are three Doppler modalities used in clinical applications: continuous-wave Doppler (CW-Doppler), pulsed-wave Doppler (PW-Doppler) and color-Doppler imaging (CDI). These three modalities are widely used to both measure and visualize blood velocities. However, Doppler ultrasound suffers from several limitations when used as a quantitative instrument. One main limitation is that the blood flow is three-dimensional, whereas Doppler velocity estimates are one-dimensional. Hence, conventional Doppler measurements are only able to estimate velocity components parallel to the ultrasound beam axis, which will result in the measured velocity being dependent on the beam-to-flow angle.

Many techniques designed to estimate two or three velocity components have been proposed to improve applications based on Doppler ultrasound, in order to achieve accurate, angle-independent velocity estimates. However, these techniques not yet widely used in clinical practice as they suffer from several limitations. One of the most fundamental challenges of these techniques is aliasing of velocity estimates, meaning that the maximum measurable velocity is limited by the pulse repetition frequency (PRF). In previous work, we have developed a new, computationally cheap, method for aliasing-correction of Doppler estimates, which was validated using a research scanner acquisition, recording data from a healthy volunteer and from a patient with stenosis. The method resulted in reliable vector velocity estimates for high velocities.

In this work we aim to investigate the potential of this method in a duplex acquisition setup, in which the ultrasound scanner rapidly switches between a Doppler sequence and a sequence designed to produce high quality anatomical images for navigation. This could result in a future real-time application with aliasing corrected Vector Doppler estimates and high quality B-mode images, with one of the potential challenges being the limitations in packet size. First, method parameters are optimized using simulations. Then, the performance of the method is assessed using a phantom study. Finally, feasibility of the method *in vivo* is demonstrated using healthy volunteers.

Chapter 2

Background

This chapter contains background knowledge that can be found in many medical ultrasound textbooks and works. It provides the necessary information for the reader to understand this work. Please refer to [2]-[33] for more details.

2.1 Medical Ultrasound imaging

Ultrasound imaging is based on transmitting ultrasound pulses, which are pressure waves with high frequency, through a medium.

The propagation of a pressure wave, $p(r, t)$, is described using the wave equation:

$$\nabla^2 p(\mathbf{r}, t) - \frac{1}{c^2} \frac{\partial^2 p(\mathbf{r}, t)}{\partial t^2} = 0, \tag{2.1}$$

where t is the time, $\mathbf{r}$ is spatial position and c is the speed of sound. This equation implicitly assumes that the medium of propagation is homogeneous, and that the speed of sound is constant.

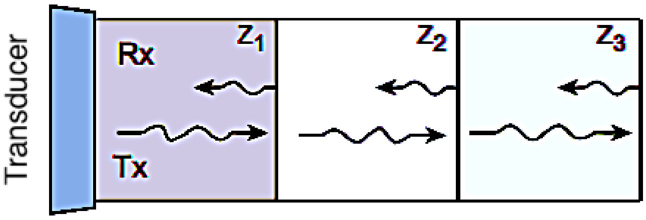

Figure 2.1: An illustration of the pulse-echo principle. An ultrasound pulse is transmitted into the tissue, and is reflected at interfaces between different types of tissue Z1, Z2, and Z3. The reflected echoes will arrive back at the transducer surface at different time points.

Properties of the medium that influence the propagation of waves include density and compressibility. Equation (2.1) shows that propagation properties in a homogeneous medium will be along a spherical wavefront extending from the source. However, for an non-homogeneous medium the propagation properties will be dependent on the acoustic impedance, Z, given by:

$$Z = \rho_0 c, \tag{2.2}$$

where ρ_0 is the density of the tissue and c is the speed of sound. In diagnostic ultrasound the transmitted wave will propagate through different tissues with different acoustic impedance within the human body. Changes in acoustic impedance will result in the wave being scattered or reflected back, depending on the size of the object. Scattering is referring to an interaction between waves and particles that are small compared with the wavelength λ, in which case the backscattered echoes will propagate in all directions away from the scatterer. Ultrasound images are produced assuming that the received signal is the result of scattering.

If the ultrasound waves interfere with objects which are large compared to the wavelength, the wave will be reflected. In this case, the ratio R between transmitted and reflected pressure amplitude is dependent on the accoustic impedances Z_1 and Z_2 of the medium and object, respectively:

$$R = \frac{Z_2 - Z_1}{Z_2 + Z_1} \tag{2.3}$$

By assuming a constant speed of sound c, the distances between the transducer and any object in the body can be calculated, using the following relation:

$$z = \frac{ct}{2}, \tag{2.4}$$

where t is the time difference between the beam transmission and backscattered echo reception. Image formation based on this equation is typically referred to as pulse echo imaging.

2.1.1 Ultrasound pulses

An ultrasound image is produced from transmission of several ultrasound pulses with short length in rapid succession. A pulse usually refers to the physical pressure wave emitted by the transducer, whereas a beam is the abstract spatial region which is insonated by a pulse.

In order to avoid interference between echoes, the time between transmitted pulses should be longer than the time it takes for the pulse to travel to depth z and back:

$$\frac{1}{\mathrm{PRF}} > 2\frac{z}{c}, \tag{2.5}$$

where PRF is the number of pulses transmitted by the transducer per second, and is referred to as the pulse repetition frequency. Usually, the PRF is between 1-20 kHz in diagnostic imaging.

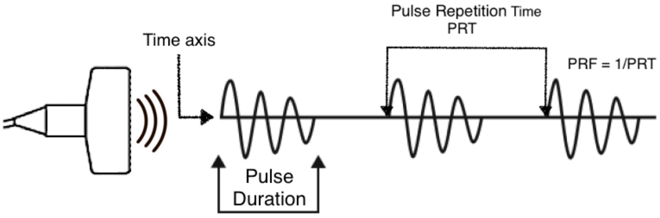

Figure 2.2: Illustration of ultrasound pulses generation

As the transmitted ultrasound signal propagates and travels further through tissue, it will be gradually attenuated due to absorption. The signal attenuation depends on tissue properties, but increases with increasing depth and increasing frequency. For soft tissues, 0.5-0.7 dB/cm/MHz is typically used as an absorption coefficient.

2.1.2 Transducers

Most commercial medical ultrasound scanners today produce images using a transducer with piezoelectric elements. Transducers are necessary for transmitting and receiving the ultrasound pulses. There are several transducer types for different diagnostic applications, where the transducers differ in shape, see Figure 2.3. Today, most commercial transducers consist of an array of piezoelectric elements which can be excited individually.

Transducers are designed with different operating center frequency and bandwidth, depending on penetration and resolution requirements of the medical application.

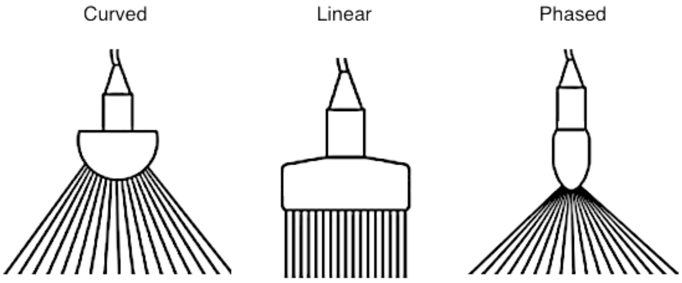

Figure 2.3: An illustration of the three different medical ultrasound transducers and the beam directions typically used.

The piezoelectric elements of a transducer produce an ultrasound pulse on transmission as they vibrate in response to an external electric field. The pulse will propagate through surrounding tissue and into the body, and because of inhomogeneities in the body, echoes will be backscattered to the transducer, where they are received by the transducer elements and converted back to electrical signals.

The application of interest in this work is vascular imaging. In this application, typically a linear array is used, where the piezoelectric elements are all positioned along a straight line. When performing a linear scan, a subset of the elements are used for transmission and reception of each ultrasound beam. By modifying the subset of elements, the beam is swept along the lateral direction. The beams are all parallel and for each transmit a scan line is formed, producing a rectangular image.

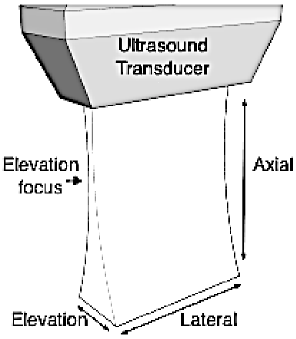

Figure 2.4: Illustration of the axial, lateral and elevation directions

Figure 2.4 shows the directions of an ultrasound image. Both axial and lateral directions are in the image plane, where the axial direction is the direction of pulse propagation and the lateral direction is parallel to the long axis of the transducer. The elevation direction is perpendicular to the image plane.

2.1.3 Image formation

There are two ways of performing focused ultrasonic scanning using a transducer. The first one is to steer the ultrasound beams in different directions, as is the case for the curvilinear and phased arrays. The other alternative is to use different parts of the aperture to move the beam in the scanning direction, as is typically the case for the linear array.

2.1.3.1 IQ-demodulation

The signal received by the transducer is a real-valued RF signal with high sampling frequency. Reducing the amount of data of the received signal is often desired, therefore an intermediate step in the ultrasound processing that is applied in this case, is IQ-demodulation.

IQ-demodulation reduces the amount of data without losing information. IQ-demodulation can be done by first applying the Hilbert transform getting the pre-envelope and then down-mixing to bring the signal to the baseband:

$$x_{IQ}(t) = H(x_{RF})(t) \exp\left(-2\pi i f_d t\right), \tag{2.6}$$

where H denotes the Hilbert transform, t is the time along the beam and f_d is the demodulation frequency. The remaining frequency components should be centered around the zero frequency. Because of the reduced bandwidth, the signal may now be resampled using a lower sampling frequency.

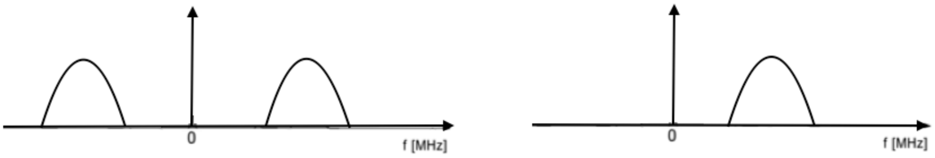

The real valued RF signal multiplied with a complex sinusoid signal

Negative frequencies are removed

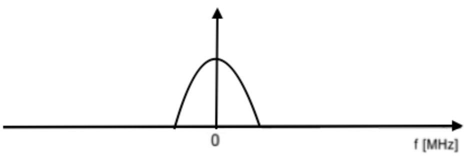

The center frequency is shifted down to zero

Figure 2.5: An Illustration of IQ demodulation, first the Hilbert transform is applied to remove the negative frequencies. Then the signal is shifted down to be centered at the zero frequency.

The final demodulated signal is referred to as the IQ signal. An illustration of the steps of IQ-demodulation is shown in Figure 2.5.

2.1.3.2 Beamforming

When scanning, it is desirable to control where in space the transmitted ultrasound pulse propagates. When transmitting an unfocused pulse, the signal from different elements will arrive at any given point on different times. Hence a delay profile is applied to the transducer elements to ensure that all pulses reach the focus point simultaneously. Similarly, at reception, when the pulse is scattered back from a scatterer in the body, the backscattered pulse waves will propagate radially away from the scatterer, hitting the transducer elements at different time points. Hence, a new delay profile is applied considering the two-way propagation time between the transducer and the focus point.

The time a transmitted pulse takes to travel from the transducer to an image point and back to the transducer is referred to as time-of-flight (ToF). For a linear scan without steering, with probe element i positioned at $(e_i, 0)$ the ToF is given by:

$$ToF(x,z,i) = ToF_{TX}(x,z,i) + ToF_{RX}(x,z,i) = \frac{z + \sqrt{(x-e_i)^2 + z^2}}{c} \tag{2.7}$$

For each pixel (x,z) in the image, the signal from all elements are interpolated at time corresponding to ToF(x,z,i), and summed to produce the ultrasound image. This process is referred to as beamforming, Figure 2.6 illustrates the beamforming concept on receive.

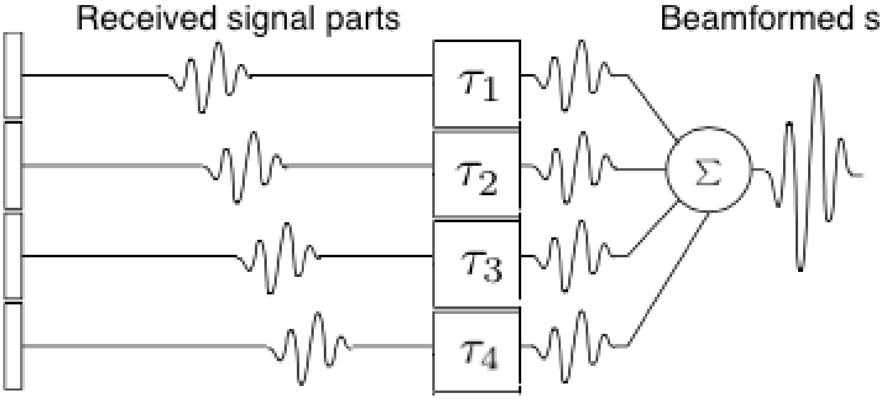

Figure 2.6: Illustration of the beamforming concept on reception. The received signals are time-delayed individually for each channel so that they add up coherently.

According to the Fraunhofer approximation, the field variation in the focus depth is proportional to the Fourier transform of the aperture weighting function. Which means that, for a rectangular aperture where all elements have equal weighting, the one-way pressure beam profile p at the focus depth is approximately given by:

$$p = \operatorname{sinc}(\frac{x}{f_{\#tr}}\lambda), \tag{2.8}$$

where K is a proportionality constant, λ is the wavelength and $f_{\#tr}$ is the ratio between the transmit focus depth z and the diameter of the aperture D,

$$f_{\#tr} = \frac{z}{D} \tag{2.9}$$

The sinc function in equation 2.8 has a main lobe and side lobes that are only 13 dB weaker than the main lobe. The field in the focus depth will then be composed of a main lobe and surrounding side lobes. By weighting the elements with an apodization window, the side lobe level is reduced, at the cost of a slightly wider main lobe. Without apodization, the width of the main lobe may be approximated as:

$$D_f = f_{\#tr}\lambda \,, \tag{2.10}$$

Another way to define the beam width is the full width at half maximum (FWHM) of the pressure amplitude. The FWHM can be found as the lateral distance between the field points with amplitude 3 dB lower than the peak amplitude. An approximation for the FWHM is:

$$\text{FWHM} = 1.2 f_{\#tr}\lambda \tag{2.11}$$

The two-way beam profile depends on the $f_{\#}$ on both transmit $f_{\#tr}$ and receive $f_{\#rc}$ and can be calculated as:

$$f_{\#} = \frac{f_{\#tr} f_{\#rc}}{f_{\#tr} + f_{\#rc}} \tag{2.12}$$

The lateral width of the two-way beam is given by:

$$D_f = f_{\#}\lambda \tag{2.13}$$

2.1.4 Image quality

In this section we briefly describe important quantitative measures of image quality in ultrasound, and important factors that degrade image quality.

2.1.5 Image quality parameters

Spatial resolution

The spatial resolution is the minimum distance between points that can be discovered, and is limited by spatial smearing in the image. The spatial resolution in an ultrasound image depends on several factors. Both the elevation and lateral resolution depends on the $f_{\#}$ in those directions and the wavelength, as can be seen in Eq. 2.13. If the frequency is increased, the wavelength decreases, the beam width decreases, and lateral resolution is improved. The axial resolution, on the other hand, depends on the pulse duration, where axial resolution is better the shorter the duration of the pulse is.

Focusing is a main factor to increase image quality as it improves signal strength and increases image resolution both in lateral and elevation directions. In the elevation direction mechanical focusing is typically performed, using either curved transducer elements or a lens in front of the transducer surface. In the lateral direction, focusing is typically achieved electronically by applying delays to the transducer elements, as described in the previous section.

Contrast

Another measure of image quality is contrast, which is defined as the ability to differentiate between two regions with different acoustic properties in an ultrasound image. Essentially, contrast depends on image resolution and the ratio between the main lobe and sidelobes of the beams.

Signal-to-noise ratio (SNR)

In addition to the backscattered echoes from scatterers, the received signal will contain electronic noise from the measurement system, as well as noise caused by random motions in the medium.

If the noise amplitude is comparable or larger than the signal amplitude, it will lead to severe degradation of images and velocity estimates. One of the most important measures of signal quality is therefore the ratio between the power of the signal, and the power of noise; the signal-to-noise ratio (SNR).

The SNR in decibels may be calculated using the following equation:

$$SNR_{dB} = 20 \log_{10} \frac{P_{signal}}{P_{noise}}, \tag{2.14}$$

where P is the power.

The power of the received signal is proportional to the power during transmission, whereas the noise level is independent of it. Therefore, an increase in transmit power will improve the SNR. However, the transmit power one may use is limited by patient safety regulations. Too much transmitted power can cause tissue damage due to heating, as the transmitted energy into the body will be absorbed and result in an increase in temperature.

2.1.5.1 Corrupting factors

There are several factors that may reduce image quality. Typically, this happens because the speed of sound is conventionally assumed to be constant. However, due to inhomogeneities in the body, the speed of sound will vary. Hence, the image quality will end up being degraded because of several factors mentioned below.

Refraction

When a wave crosses a boundary between two media, the wave might change direction depending on the difference in acoustic impedance in the two media. This may lead to degradation in resolution and artifacts.

Aberrations

The variations in the sound speed will also distort the wavefront of the transmitted beam, which will lead to defocusing and lateral blurring in the image. This phenomenon is referred to as wave front aberration. As a consequence, the main lobe will expand, and the level of side lobes will increase.

Reverberations

Another fundamental assumption is that scattering occurs only once when the wavefront from the transducer passes the scatterer. This is not valid in the case of reverberations, in which case the wavefront is reflected multiple times during propagation, typically between the surface of the skin and the transducer. Reverberations will produce blurred copies of objects below their true locations in the image.

2.1.6 Display modes

Images generated by ultrasound may have different display modes. There are two major tissue modes, which are the B-mode (brightness mode) and the M-mode (motion mode). The most used one is the B-mode, which generates a two-dimensional image from the received backscattered echo, color coding the received signal power using gray scale levels. An example a B-mode image is shown in Figure 2.7.

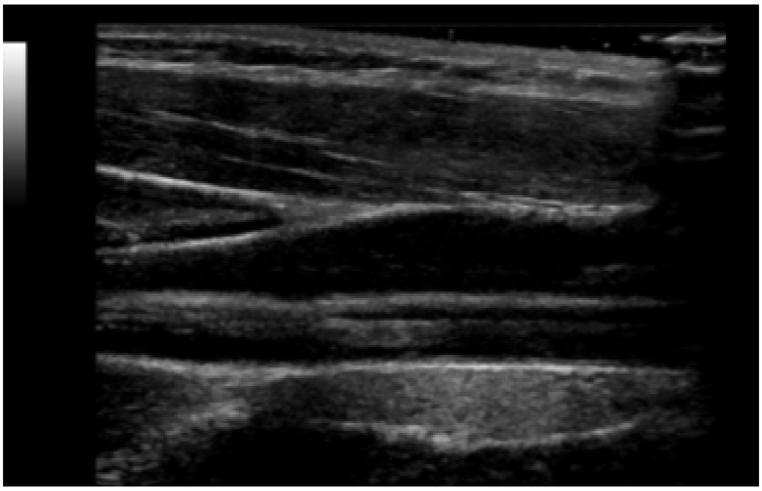

Figure 2.7: B-mode image of artery

In order to be able to produce a useful B-mode image of objects high spatial resolution is required. It is also useful to have a high frame rate in order to investigate the dynamics of the structures.

To assess cardiovascular disease, B-mode images are used for navigation before using Doppler modalities to assess blood velocities.The Doppler modalities include continuous-wave Doppler (CW-Doppler), pulsed-wave Doppler (PW-Doppler), and color-Doppler imaging (CDI). These techniques are today widely used to visualize and measure blood velocities in the cardiovascular system. A more detailed description of blood flow imaging is given in the next section.

2.1.7 Plane wave imaging

In modern ultrasound systems, the whole region of interest may be insonated with a single transmission using plane waves. This is referred to as plane-wave imaging and is based on transmitting an unfocused beam using the full aperture. The plane-wave modality is also referred to as ultrafast ultrasound imaging because it can generate a B-mode image using few transmissions, thus achieving a high frame rate. Figure 2.8 shows an example of the transmit and receive beams used in plane wave imaging.

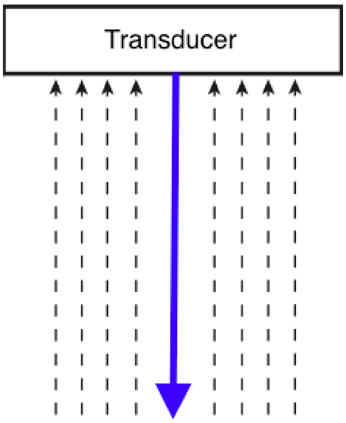

Figure 2.8: An illustration of the single wide transmit transmit beam (the blue arrow) and the multiple receive beams (dashed arrows) used for plane wave imaging.

The first plane-wave imaging experiment for B-mode imaging was described by Delannoy [10] in 1979, and later it has been applied to blood flow imaging [11]. However, there are some drawbacks of using the plane-wave modality as it reduces both penetration, due the limitation of transmit focusing, and the lateral resolution. However, these challenges may be overcome by using multiple overlapping plane wave transmissions with different steering angles and doing coherent compounding [13], meaning that all the complex low-resolution images are summed to produce a high-resolution image.

2.2 Blood flow imaging

Ultrasound imaging has become an important tool to image and quantify blood flow in the heart and arteries. A standard modality that is used in this context is Doppler imaging, which may be used to show the the distribution of flow velocities in a region of interest (ROI).

Doppler modalities are based on the frequency shift a wave is exposed to when it is scattered back from a moving scatterer. The corresponding shift in frequency, f_d, is given by the Doppler equation:

$$f_d = 2f_0 \frac{v \cos\theta}{c}\,, \tag{2.15}$$

where f_0 is the emitted frequency, v is the the velocity of the moving scatterer and θ is the angle between the ultrasound beam and the velocity direction of the scatterer. The Doppler effect will result in a frequency shift in waves as they are scattered by a moving object. Equation (2.15) is valid as long as $v\,\cos\theta \ll c$. The blood velocities for a person with healthy carotid arteries, will usually range up to $1\,\mathrm{m/s}$ for normal flow. However, higher blood velocities may be present near a stenosis or narrowing in a blood vessel.

As noted earlier, there are three modalities that are referred to as Doppler based: continuous-wave (CW) Doppler, pulsed-wave (PW) Doppler and color-Doppler which is also referred to as color flow imaging (CFI). Both CW- and PW-Doppler are modalities that provide the velocity distribution of blood in a sample volume, whereas color Doppler provides a mean velocity map in a larger region of interest. In the following, PW Doppler and CW Doppler modalities are described briefly, before describing CFI in more detail.

2.2.1 Continuous-wave Doppler

Continuous wave Doppler uses the Doppler effect, as described above. The transmitting aperture sends a continuous sinusoidal wave through the medium, which may be written:

$$e(t) = \cos(2\pi f_0 t) = Re\{e^{i2\pi f_0 t}\} \tag{2.16}$$

where f_0 is the transmitted frequency. After demodulation, the received signal will have frequency content corresponding to the Doppler shift produced by all insonated moving scatterers.

Figure 2.10 shows a schematic of a simple CW Doppler instrument, where the transducer aperture is divided into two parts. Half the transducer aperture is used to continuously transmit an ultrasound beam into the tissue, and the other half is used to simultaneously receive the backscattered echo from moving scatterers.

The sample volume in CW-Doppler systems is defined by the overlap region between the transmit and receive beams, and the resulting Doppler shift will be proportional to the axial velocity component. Doppler shifts from all moving scatterers in the overlap region are observed. The region of overlap will usually be long, leading to a lack of range resolution. The main advantage of using the CW-Doppler modality is that it is not limited by a maximum measurable velocity as is the case for other Doppler modalities. Hence, it does not have any aliasing problems.

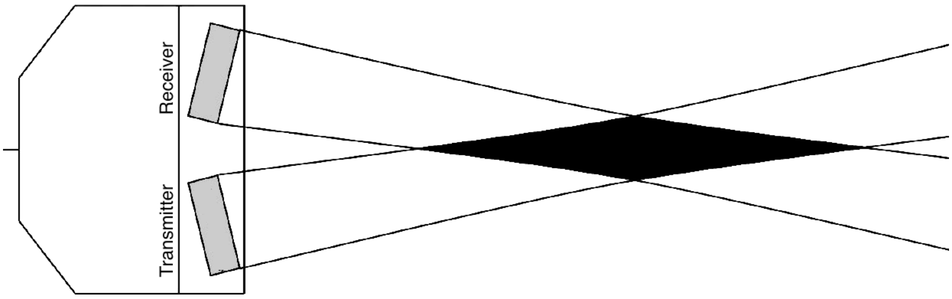

Figure 2.9: An illustration of a simple CW-Doppler instrument. An ultrasound wave is transmitted continuously into tissue using one part of the transducer aperture, whereas the other part is used to receive the backscattered signal.

2.2.2 Pulsed-wave Doppler

In pulsed-wave Doppler, several pulses are transmitted into the body with a constant pulse repetition frequency. Unlike continuous-wave Doppler, the same transducer aperture may be used to both transmit and receive the ultrasound beams, similar to the B-mode modality. As the pulses interact with moving scatterers, it will cause a shift in the pulse center frequency, according to (2.15). However, measuring the change in pulse frequency caused by the movement of scatterers is not easy because the Doppler shift is small compared to the bandwidth of the pulse, and because the received frequency depends also on attenuation. However, phase changes in the backscattered echoes between consecutive pulse transmissions are measured instead. A transmitted pulse consists of sinusoidal oscillations given by:

$$e(t) = g(t)e^{i2\pi f_0 t}, \tag{2.17}$$

where f_0 is the transmitted pulse frequency and $g(t)$ is the complex envelope of the pulse.

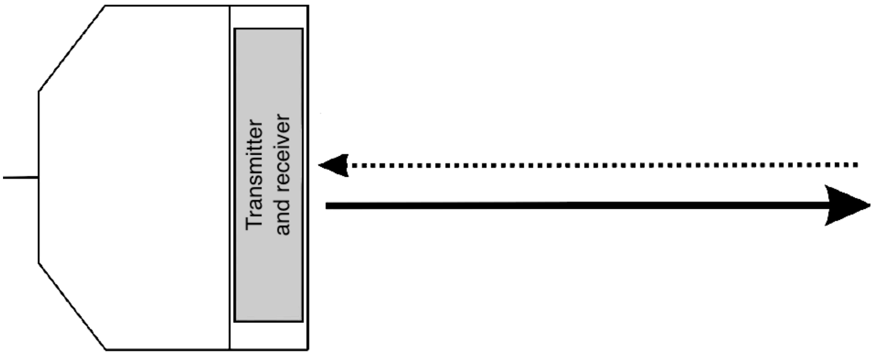

Figure 2.10: An illustration of a PW-Doppler instrument.

The backscattered signal from each pulse is sampled with high sampling frequency, typically 40-80 MHz, and this signal dimension is commonly referred to as the fast-time dimension. By sampling the signal at a specific depth or spatial point across several firings, we obtain a slow time signal. The sampling frequency of this signal is equal to the pulse repetition frequency, which is typically 1-20 kHz. An illustration of this is given by Figure 2.11.

After demodulation, the slow time Doppler signal is complex, with frequency content dependent on the axial velocity distribution.

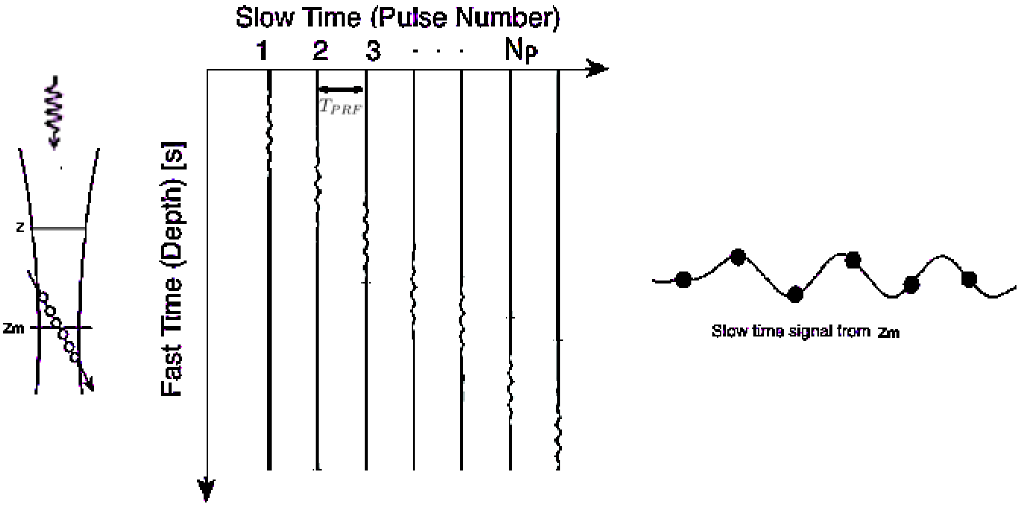

Figure 2.11: An illustration of fast time and slow time signals from a scatterer moving through the ultrasound beam. The slow time signal sampled at depth z_m will look like a resampled version of the fast time pulse, with sampling rate depending on the scatterer velocity.

The PW modality typically has low complexity and high robustness, also when signal-to-noise ratio is low. The main purpose of using the pulsed-wave Doppler modality is to extract the blood velocity distribution from a small sample volume in a vessel or in the heart. This will be possible because the use of a pulsed transmission with focusing results gives us both range resolution and lateral resolution.

However, PW Doppler suffers from several limitations, one of which is transit time broadening. This limitation becomes more severe the larger the angle between the transmitted ultrasound beam and the blood flow direction is. In addition, the slow time spectral bandwidth increases with higher velocities. Transit time broadening may result in reduced accuracy of the blood velocity estimates, and may overrun details in the spectral display.

Another important limitation of PW Doppler, is that the maximum measurable velocity along the beam axis is limited by the pulse repetition frequency. In conventional PW Doppler the time interval between firings must be at least $T = 1/PRF$. If the Doppler shift exceeds PRF/2, aliasing in the Doppler spectrum will occur. The corresponding maximum measurable velocity is referred to as the Nyquist velocity and is given by:

$$v_{Nyquist} = \frac{c\,\mathrm{PRF}}{4f_0} \tag{2.18}$$

Velocities higher than the Nyquist velocity will be aliased onto lower velocities.

2.2.3 Color Flow Imaging

Both PW and CW Doppler are used to quantify blood velocities from a small region of interest. Color Flow Imaging (CFI), or Color Doppler imaging (CDI), on the other hand, is a modality that is used to display mean blood velocities in a 2-D or 3-D region of interest.

CDI is often combined with CW or PW Doppler. This combination is very useful in vascular imaging: CDI provides the spatial distribution of blood velocities and has the ability to detect the abnormal blood flow region, whereas PW Doppler may be used to estimate the velocity distribution in a smaller region of interest.

The conventional way of performing color flow imaging is by using a modified scan sequence, where several focused beams are transmitted successively in each beam direction, with a certain pulse repetition frequency. The velocity estimates are then built line-by-line, as illustrated in Figure 2.12.

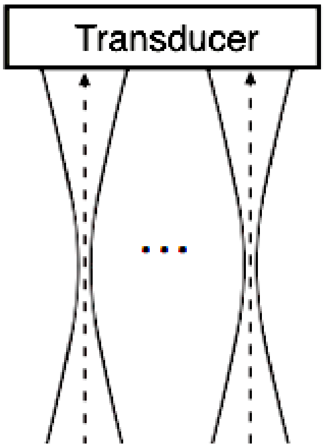

Figure 2.12: An illustration of receive lines generated with line-by-line imaging scheme.

However, conventional CFI has several limitations. In order to achieve a good impression of the blood flow and be able to observe changes in blood velocities, several consecutive transmissions with long pulses are required. This becomes a trade off because a longer pulse leads to lower axial resolution.

Another limitation is the frame rate. It is preferable to have a high packet size in order to achieve accurate blood velocity estimates. This leads to a trade-off between image quality, the size of the color flow image, and the frame rate. It is also desirable to have as few transmissions as possible, since the number of lines needed to produce the image will limit the achievable frame rate.

Figure 2.13 shows a block diagram of CFI processing, and a more detailed description is given in the following subsections.

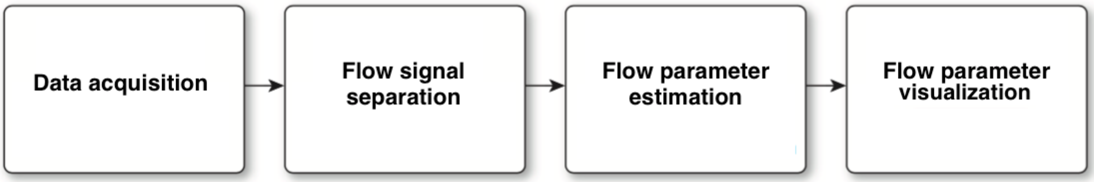

Figure 2.13: Block diagram of CFI processing.

2.2.3.1 Clutter Filtering

Blood signal separation is important in color flow imaging. Due to beam side lobes and reverberations, echoes from slowly moving tissue will be in the same pixels as the signal from blood. Hence, attenuating the echoes from tissue is necessary in order to detect blood and be able to estimate the blood velocity. The challenge is that the signal from tissue is typically 40-60 dB stronger than the signal from blood. However, blood moves with higher velocities than tissue. In conventional CFI, the clutter signal from tissue is typically removed by applying a high-pass filter in the slow-time domain. The filter should have high stop-band attenuation to be able to remove the strong clutter component, and a short transition region to minimize removal of the Doppler signal from blood. An example of a filter frequency response is shown in Figure 2.14.

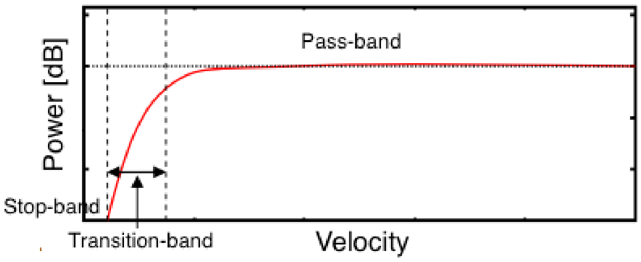

Figure 2.14: Illustration of a clutter filter frequency response.

For clutter filtering in CFI there are several filter types that can be used, including FIR filters, IIR filters and polynomial regression filters.

Finite Impulse Response Filter

Finite impulse response (FIR) filters are time-invariant and have finite impulse responses. The FIR filtering process can be described using the impulse response function $h(n), n = 0, 1, ..., M-1$, with length M, and the input signal $x(k), k = 0, 1, ..., N_p$, where N-p is the number of samples. The output signal $y(k)$ is given by the convolution sum:

$$y(k) = \sum_{n=0}^{M-1} h(n)x(k-n) \tag{2.19}$$

FIR filters are easy to implement with low computational complexity. However, discarding initial samples is necessary after filtering. FIR filters will therefore reduce the number of samples left for velocity estimation, yielding increased variance in CFI. Therefore, the filter length should be short in order to avoid discarding too many samples.

Infinite Impulse Response Filter

Infinite impulse response (IIR) filters are time-invariant and has an output signal given by:

$$y(k) = \sum_{k=1}^{M} -a_k y(n-k) + \sum_{k=0}^{M} b_k x(n-k), \tag{2.20}$$

where a_k and b_k are the filter coefficients. This is a recursive equation, where the output samples depend on the present and past input samples $x(n)$ as well as past output samples $y(n)$. Similar to FIR filters, filtering using IIR filters will result in distortion of the initial samples. To reduce such effects, filter initialization is used, meaning that the start of the signal is padded before filtering. This is especially important for CFI as the input signal is of relatively short length. There are different methods that have been proposed for initialization of IIR filters.

Polynomial Regression Filters

Polynomial regression filters are linear, time-variant filters that model the clutter signal as a linear combination of slowly varying polynomial basis functions. The coefficients of the polynomials are determined by a least squares fit. Then the M components with lowest order are subtracted from the signal. The output of the filter is given by:

$$y = (I - \sum_{n=0}^{M-1} b_n bn^H)x\,, \tag{2.21}$$

where M-1 is referred to as the order of the polynomial filter, b_k are orthonormal basis vectors spanning the clutter signal subspace, I is the identity matrix and H denotes the conjugate transpose.

Polynomial regression filters do not require initialization, leaving more temporal samples for velocity estimation compared to FIR and IIR filters. In addition polynomial regression filters have narrower transition regions compared to FIR and IIR filters with the same order. However, because the filters are time-variant, it is more difficult to define the frequency response compared to FIR and IIR filters [23].

2.2.3.2 Blood velocity estimation

To estimate the mean blood velocities in CFI, the autocorrelation approach is typically used. This approach is based on estimating a phase-shift at a given pulse frequency between successive slow-time samples. It was first introduced by Nakemawa and Kasai for diagnostic ultrasound applications in the mid-1980s, resulting in the first real-time two-dimensional CFI system [16]. The estimator uses the lag 1 autocorrelation of the signal, given by:

$$\hat{R}(1) = \frac{1}{N_p} \sum_{k=0}^{N_p-1} x(k)^* x(k+1), \tag{2.22}$$

where x is the slow-time signal, N_p is the number of slow-time samples, and * denotes the conjugate operation. The mean axial velocity of blood is further obtained by the following equation:

$$v_z = \frac{\angle \hat{R}(1)\, PRF_c}{4\pi f_0}, \tag{2.23}$$

where f_0 is the received pulse center frequency. The velocity estimator is prone to aliasing, and the maximum measurable velocity is given by the temporal sampling frequency as shown in equation (2.18).

The autocorrelation approach is based on estimating the mean velocity from the phase shifts between sequential slow-time samples. The variance of the estimates increases with the bandwidth of the slow-time spectrum. Another approach, called the cross-correlation approach, estimates the time delay between the fast time signals from successive transmissions. Several velocity approaches have been proposed since color flow imaging was put into use, including the maximum likelihood estimator and many others. However, the autocorrelation is the approach used in this work.

2.2.3.3 Blood velocity visualization

Arbitration

On display, ultrasound images produced in CFI are normally overlaid on a B-mode image. For each image pixel, arbitration is used to decide whether to display blood or tissue by evaluating the power and frequency content of the signal.

When doing arbitration, high frequencies in the Doppler signal indicates a pixel containing blood, whereas high power in the B-mode image indicates a pixel containing tissue. Information from the B-mode image is used to reduce potential artifacts due to limitations the CFI suffer from, such as non-ideal signal separation during clutter filtering, causing signals from tissue to pass through the filter.

Visualization

The estimated blood flow velocity parameters are typically color-encoded on display. The simplest visualization is a one-dimensional color scheme, where only the mean blood velocity is color-coded. In this type of CFI visualization, the blood flow towards the transducer is color-encoded in red, and blood flow away from the transducer in blue.

Due to the spatial extent of the point spread function the tissue and flow information will necessarily overlap near the boundaries between the two. This will result in flow signal covering areas of tissue. This challenge becomes more severe if the spatial resolution of the blood flow image is reduced. Unfortunately, long pulses are typically used for CDI to improve sensitivity and reduce variance in velocity estimates, causing reduced axial resolution.

2.3 Vector velocity imaging

CFI, PW and CW modalities are all one-dimensional modalities. This means that they are only able to measure the axial velocity, whereas the true blood flow is three-dimensional. This is a major limitation as the measured velocities will be beam-to-flow angle dependent. Blood in the vessels moves parallel to the skin surface, resulting in the dominant flow direction being almost orthogonal to the ultrasound beam. When the beam-to-flow angle approaches 90 degrees, the velocity estimates will also suffer from high variance.

In the PW Doppler modality, it is possible to angle-correct the axial velocity as the blood direction can be estimated based on information from CDI or the B-mode image. CFI estimates have typically been used only qualitatively and have not been angle-corrected, but there are several techniques that have been proposed in this context to remove angle-dependency and estimate both the axial and lateral velocity components.

Vector Doppler imaging

One technique that has been proposed to provide angle-independent velocity estimates in CFI is vector Doppler imaging, which is also the technique of interest in this work. Vector Doppler is a modality based on obtaining several Doppler measurements from different angles and combining velocity estimates from all angles to obtain a vector velocity estimate.

Vector Doppler imaging has been a topic of interest in the ultrasound community for about 40 years. It was proposed for the first time in the 1978 [26], where two crossed beams were used on receive to produce a two-dimensional velocity map. Other variations of Vector Doppler have also been proposed, including combining two or more images from transmissions that are steered in different directions, which is the the method of choice in this work. An advantage of using several transmit angles is that lateral resolution gets improved.

In the cross-beam approach, the beam is transmitted straight down without steering, and a split aperture is used on reception. This approach requires at least two estimates of Doppler shift from two different directions, where the velocity vector is found from the velocity components by using triangulation. The setup of the cross-beam approach is illustrated in Figure 2.15.

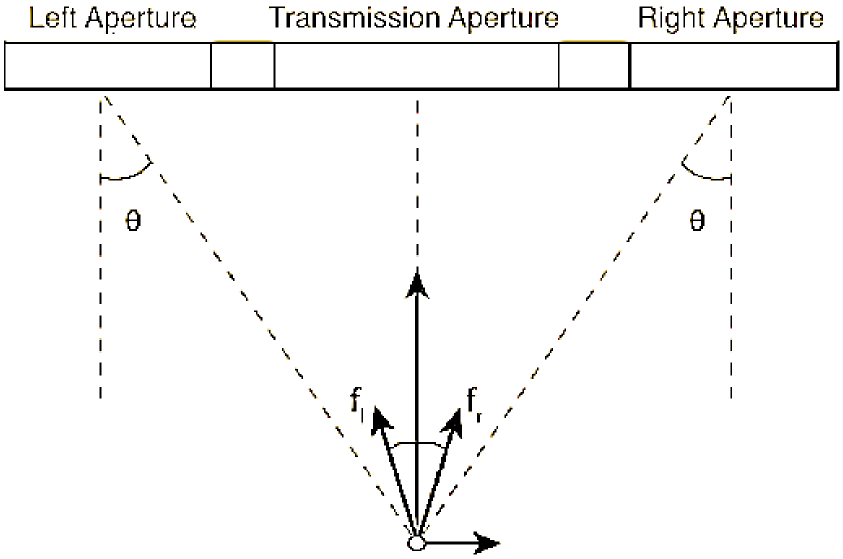

Figure 2.15: The separate subaperture approach, common transmit aperture and two separate receive apertures.

The velocity components v_x and v_z are given by:

$$v_x = c\frac{f_l - f_r}{2f_0 \sin\theta} \tag{2.24}$$

$$v_z = c\frac{f_l + f_r}{2f_0 \cos\theta}, \tag{2.25}$$

where f_0 is the center frequency of the pulse, f_l and f_r are the Doppler shifts received from the left and right aperture respectively, and θ is the angle between the transmit and receive directions. The main benefit of using the cross-beam approach is that the two directional estimates are obtained from the same transmission.

There are other alternative methods that have also been used such as the lateral modulation which is related to the cross-beam approach. In this technique, an apodization scheme is used at reception to produce oscillations in the lateral direction of the resulting image. The phase-shift technique is further used to register the scatterer movement in the lateral direction as well as in the radial direction.

Speckle tracking

There are other techniques that provide angle-independent velocity estimates, one of which is speckle tracking. The technique is based on tracking and then matching the blood interference pattern in ultrasound images. Speckle tracking was first proposed in the 1980s from Duke University [30]. Figure 2.16 illustrates the concept of speckle tracking. One of the current limitations of speckle tracking is speckle pattern decorrelation, which may occur due to e.g.non-laminar flow patterns, flow velocity gradients, and out-of-plane movement.

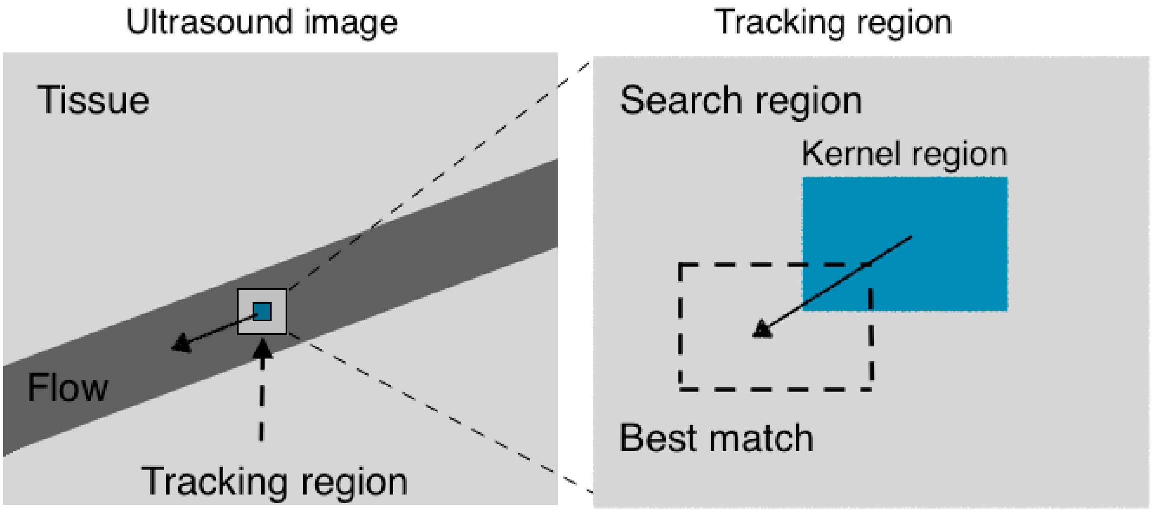

Figure 2.16: Speckle tracking schematic. The tracking region is defined, and the best match for an image kernel region is searched for in subsequent frames.

In principle, the velocity vector is estimated by determining the displacement of the blood between frames using cross-correlation of rectangular image regions. However, cross-correlation between image sections in the two-dimensional image plane, or in a three-dimensional image volume requires many calculations and is challenging to implement in real-time.

Chapter 3

Method

A new method inspired by the multiple least squares method presented in [27] was developed to detect and correct aliasing errors. Details on the vector Doppler acquisition, aliasing correction method and experimental validation are included in this chapter.

3.1 Acquisition and processing

The acquisition scheme for recordings and simulations done in this work, consisted of a B-mode sequence using 11 plane waves with different steering angles and a vector Doppler sequence using plane waves with two steering angles, fired alternately. This resulted in a total of 11+2×(Doppler packet size) transmit events per duplex frame.

The channel data were further demodulated and beamformed offline. To be able to estimate the blood velocity, the beamformed signal was filtered in slow-time to remove the signal from tissue, which, if not suppressed, may be falsely interpreted as blood signal. The autocorrelation estimator was used to estimate Doppler phase shifts, and the phase shifts were aliasing corrected as described in the following section. The corrected phase shifts were then converted to Doppler shifts and used to calculate vector velocity estimates, as described in equation (2.23).

3.2 Aliasing Correction

The 2D vector velocity estimates are usually obtained by estimating the axial velocity in the two beam directions, using the autocorrelation estimator presented in (2.22) and (2.23). However, the velocity estimates are not always reliable as velocities above the Nyquist limit presented in 2.18 are exposed to aliasing. Hence, detecting and correcting for aliasing is necessary.

To detect aliasing, a series of signals with different center frequencies, f_k^c, were produced by applying $K = 11$ different complex band-pass filters on the IQ-data along the fast-time dimension. The center frequencies of the filters were evenly spaced in a 2 MHz band surrounding the pulse center frequency. A mathematical description of the filters, h_k, is given by:

$$h_k = h\, e^{2\pi i f_k^c t}\,, \tag{3.1}$$

where h is a low-pass FIR filter with a bandwidth of 200 kHz.

In case of no aliasing after filtering using h_k, the measured Doppler shift f_k^d that correspond to the autocorrelation estimate would be given by the Doppler equation:

$$f_k^d = \frac{2v_z f_k^c}{c} \tag{3.2}$$

where v_z is the axial velocity. This means that f_k^d is proportional to the used center sample frequency, f_k^c, as long as the Doppler shift does not exceed PRF/2. When exceeding PRF/2, the Doppler shift will fold down to the interval [-PRF/2, PRF/2]. To compensate for this, first we need the following equation relating the Doppler shifts corresponding to different center frequencies:

$$\bar{f}_k^d = (f_C^d + a\,\text{PRF})\,\frac{f_k^c}{f_C^c}\,, \tag{3.3}$$

where C is such that f_C^c is the center frequency of the transmitted pulse, f_C^d is the corresponding Doppler shift and $\bar{f}_k^d$ is the expected Doppler shift if the aliasing order of f_C^d is a. The parenthesis contains the aliasing-corrected Doppler shift when the received signal has center frequency f_C^c. The expression the follows from the proportionality between the measured Doppler shift, f_k^d, and the center sample frequency, f_k^c.

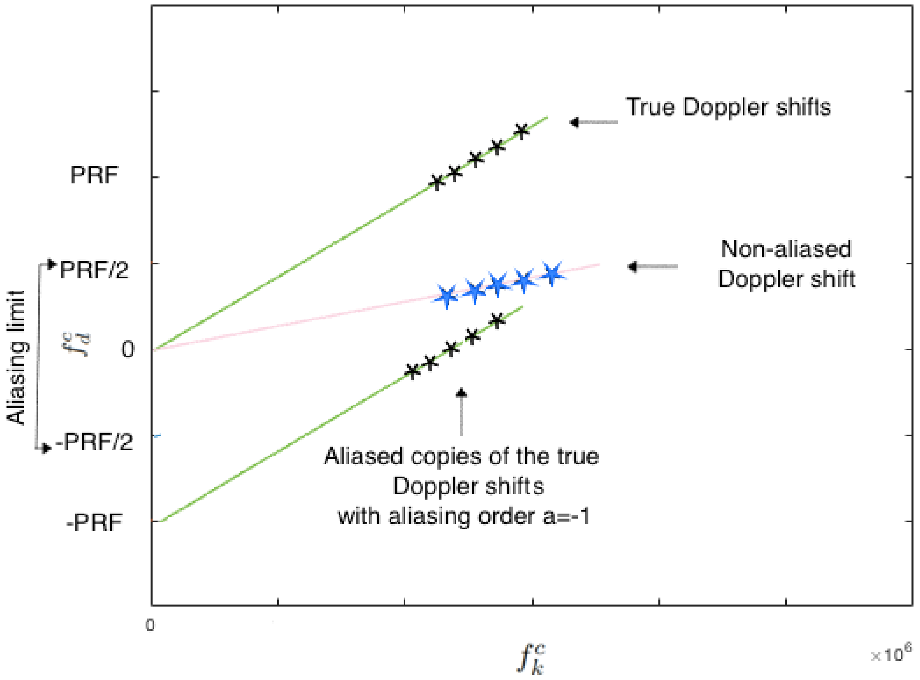

Figure 3.1: The green lines show how the true Doppler shifts fold down to the interval [-PRF/2, PRF/2] when they exceed PRF/2, but that the regression line through these points go through the point [-PRF, 0]. The pink line shows non-aliased Doppler shifts, where the corresponding line goes through [0,0].

However, the Doppler shifts $\bar{f}_k^d$ are still exposed to aliasing. If the Doppler shift frequencies f_k^d are plotted as a function of f_k^c, then in case of no aliasing all measurements should be on the line through points [0,0] and [f_C^c,f_C^d]. In case of aliasing the regression line will instead go through points [0,a PRF] and [f_C^c,f_C^d]. An illustration of this is given in Figure 3.1.

Taking into account that some, but not all Doppler shifts f_d^k may be aliased, the distance, d_k, between the expected Doppler shift and the measured Doppler shift for each aliasing order value, can be expressed as:

$$d_k = (f_k^d - \bar{f}_k^d + \frac{\mathrm{PRF}}{2})(\mathrm{modPRF}) - \frac{\mathrm{PRF}}{2}, \tag{3.4}$$

where mod denotes the modulo operation for each candidate value of a. This is further used to calculate the least squares error, e, between the measured and expected Doppler shifts:

$$e = \sum_{k=1}^{K} d_k^2 \tag{3.5}$$

Finally, the aliasing order that will result in having lowest error for image pixel, is used to correct the measured Doppler shift f_C^d corresponding to the center frequency. This is done using the following equation:

$$f^d = (\hat{f_C^d} + a\,PRF) \tag{3.6}$$

3.3 Validation

To validate and investigate the performance of the proposed correction method, a simulation study, a phantom experiment and in-vivo recordings were done.

3.3.1 Simulation study

The simulation software Field II [33] was used for channel-data acquisition. The size of the resolution cell was first calculated to select the number of scatterers, so that a normal distribution of the RF signal was achieved. In this work, 10 scatterers per resolution cell was used.

In order to imitate the blood flow conditions in the carotid artery, a simulation of a parabolic flow in a straight phantom tube was used. The output of the tube was coupled with Field II where blood was modeled as a collection of point scatterers. Plane wave acquisition was used to insonate the region of the moving scatterers with steering angles of +/- 15°. Doppler packets of different sizes were all simulated with a Doppler PRF of 6 kHz.

The tube was positioned at depth of 2 cm and angled 60° relative to the central axis of the transducer, resulting in beam-to-flow angles of 45° and 75° for the transmit and receive directions. The velocity in the center of the tube was 2 m/s.

The RF-data was demodulated, and beamforming was further performed on receive using an F-number of 1.4. Clutter filtering was further performed, using polynomial regression filters. Note that clutter filtering was not strictly necessary for the simulations, as they did not contain clutter, only blood signal. It is, however, a necessary part of the signal chain in vivo, therefore we wanted any effects of filtering to be included in simulation results. Acquisition and beamforming details are summarized in Table 3.1

Table 3.1: Simulation parameters

Probe type	Linear array
Active transmit elements	192
Transmit (Tx) frequency [MHz]	4.8
Pulse duration [cycles]	2.5
Doppler PRF [kHz]	6
Packet size	50, 100, 150
Transmit angle [deg]	[-15, 15]
Receive $f_{\#}$	1.4
Filter type	Polynomial regression
Filter order	4

Finally, the aliasing correction was performed and vector velocities were estimated, as described in section 3.2.

3.3.2 Phantom Experiment

The method was further evaluated using a phantom experiment.

An angled plane wave setup for vector Doppler acquisition corresponding to the simulation study was implemented using a Verasonics Vintage 256 scanner with a GE 9L-D linear probe. A plane wave compounding sequence with 11 angles was used to create B-mode images, followed by a Doppler sequence consisting of plane waves with steering angles -15° and 15°, which were fired alternately. Doppler packet sizes of 50, 100, 150 were used, corresponding to a total of of 111, 211, 311 transmit events per duplex frame. A firing rate of 12 kHz was used, giving approximate frame rates of 108, 57 and 39 frames per second.

The phantom was a cylindrical engine with a diameter of 32 cm that was spinning around in a water tank. Two recordings were done, one with a maximum velocity of 1.7 m/s and another with maximum velocity 2.3 m/s. An illustration of the experimental setup is shown in Figure 3.2.

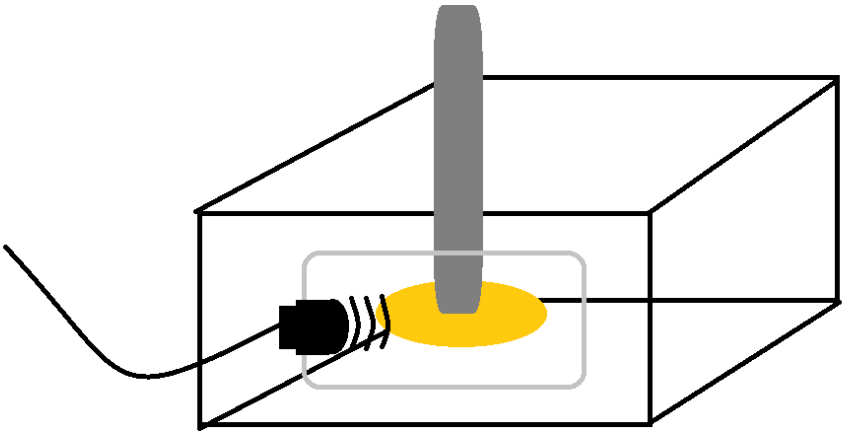

Figure 3.2: The phantom experimental setup. The Cylinder was spinning in the water tank and the probe was insonating the phantom through a silicone window.

The recorded RF channel data were further beamformed using a receive F-number of 1.4, and then demodulated. Clutter filtering was further performed using polynomial regression filters. Acquisition and beamforming details are summarized in Table 3.2. Aliasing correction was then performed using equations presented in 3.1-3.6, before estimating vector velocities using the autocorrelation estimator.

Table 3.2: Phantom setup

Probe type	Linear array
Active transmit elements	192
Transmit (Tx) frequency [MHz]	4.8
Pulse duration [cycles]	2.5
PRF [kHz]	6
Doppler packet sizes	50, 100, 150
Transmit angle [deg]	[-15, 15]
Receive $f_{\#}$	1.4
Filter order	4

3.3.3 In Vivo Recordings

In vivo data were acquired using the same setup as the phantom experiment. The probe was used to insonate the common carotid artery of a healthy volunteer.

Because the healthy volunteer did not have a stenosis and high velocities, a low Doppler PRF of 1.5 kHz was used. This was done in order to reduce the Nyquist velocity limit, so that aliasing was present in the recording

RF channel data were further demodulated and then beamformed. Clutter filtering was performed using polynomial regression filters. Aliasing correction was performed before estimating vector velocities.

3.3.4 SNR study

To investigate the performance of the method, we estimated the power of the blood signal after clutter filtering, and then added different noise signals resulting in data sets with different SNR.

Two spatial regions were defined, one containing only signal from blood, and one containing only noise after acquisition. The SNR estimate was then defined as the ratio of the mean of powers in the two regions, measured in dB.

Chapter 4

Results

4.1 Simulations

Figure 4.1 shows simulated flow from the straight tube with a maximum velocity of 2 m/s, measured using a Doppler packet size of 50, without applying the proposed method. The velocity estimates were used to generate both the color flow image and the overlaid velocity vectors.

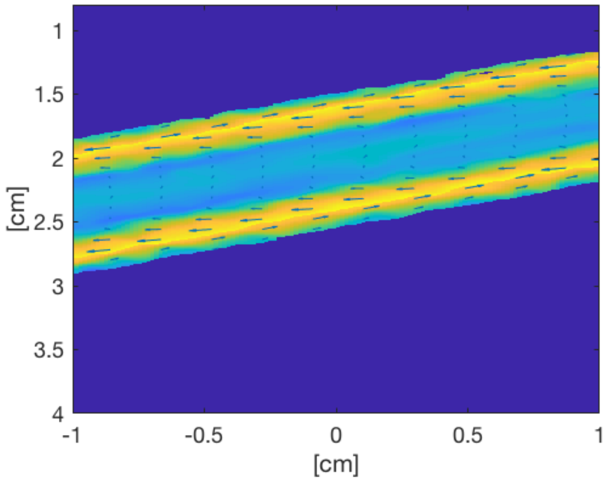

Figure 4.1: Estimated velocities from the simulated straight tube phantom using a packet size of 50, before aliasing correction.

It may be observed that the velocity profile is somehow uniform. However, the blue region shown in the image with apparently low velocities corresponds to the region of flow with highest velocities, obviously affected by aliasing. The yellow regions in the image with flow in the opposite direction (to the left) are also affected by aliasing.

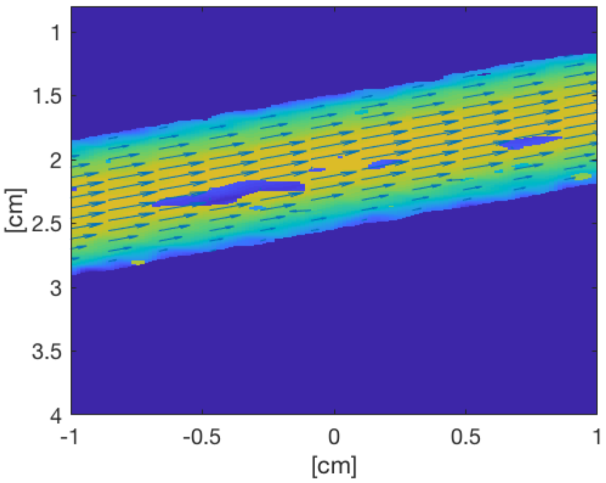

Figure 4.2: Flow estimates from the simulated straight tube phantom with a packet size of 50 after aliasing correction.

The proposed method was used to correct for aliasing, with results shown in Figure 4.2. The vector velocity field is now more uniform. However, some dropouts may be observed in the regions with the highest velocities. To reduce the variance, larger packet sizes of 100 and 150 were used so that the autocorrelation estimates could be averaged over a larger number of Doppler samples. Figure 4.3 shows the flow after the aliasing correction when using packet sizes of 100 and 150.

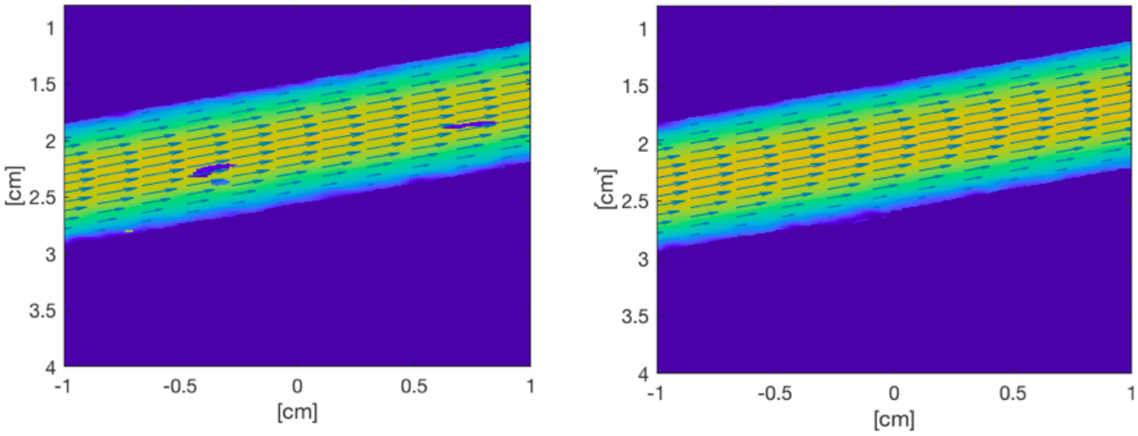

Figure 4.3: Left panel: Flow estimates from the simulated straight tube phantom with a packet size of 100. Right panel: The corresponding figure when using packet size of 150.

A better performance of the correction method may now be observed in the left panel in Figure 4.3 when using a packet size of 100. However, some dropouts are still observed. The right panel on the other hand shows robust performance of the method when using a packet size of 150. Figure 4.4 illustrates how the aliasing correction method works when using a Doppler packet size of 150.

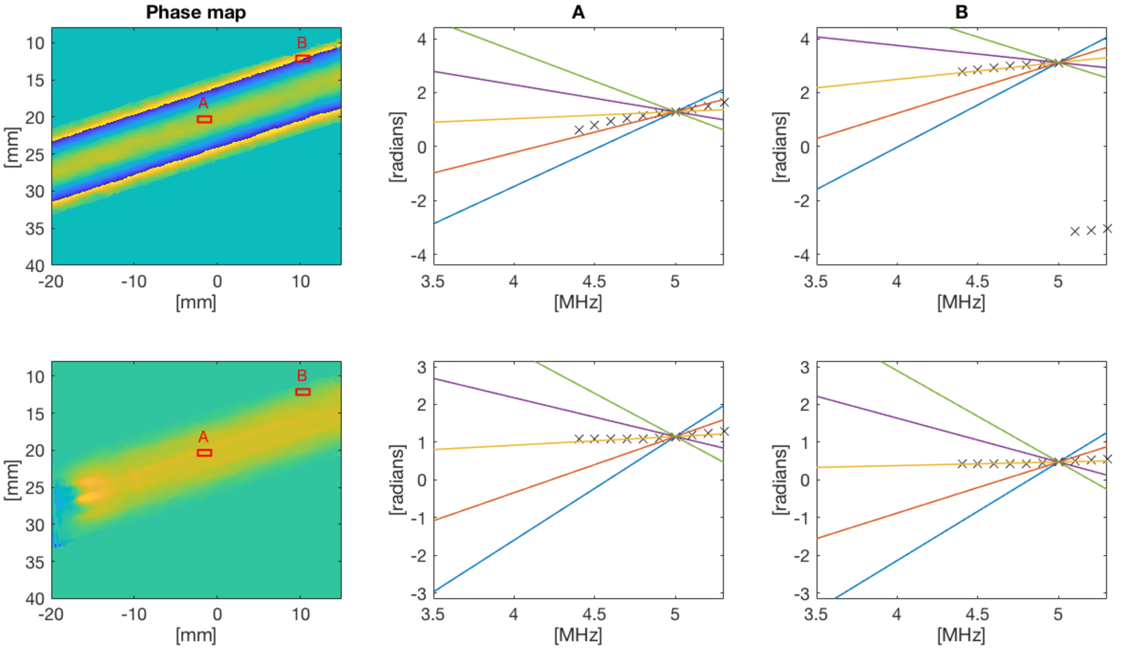

Figure 4.4: Upper panels: a map of the autocorrelation phase angle showing measured phase shift for pixel A with aliasing order 1, and for pixel B with no aliasing. The plots are showing the phase angle of the autocorrelation estimate as a function of fast time filter center frequency. Lower panels: The corresponding figures for angle 2, where both pixel A and B have no aliasing.

4.1.1 SNR-study

Figure 4.5 shows the flow from the straight tube with a packet size of 150, where a noise signal with the same mean power as the blood signal was added, yielding an SNR of 0 dB.

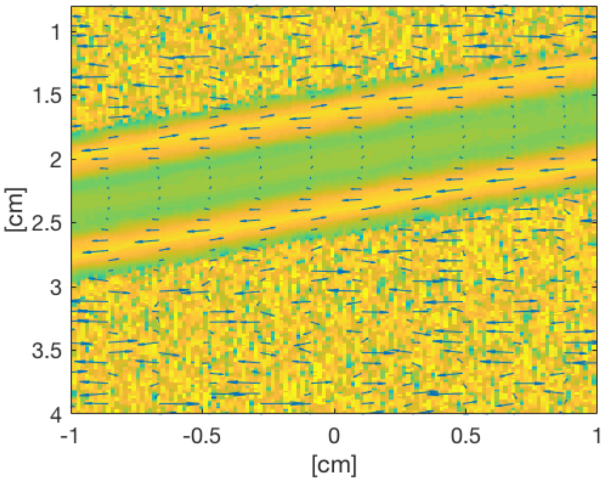

Figure 4.5: Flow estimates from the simulated straight tube phantom, with noise added such that the SNR is 0 dB.

Figure 4.6 shows the flow with noise added, after applying aliasing correction.

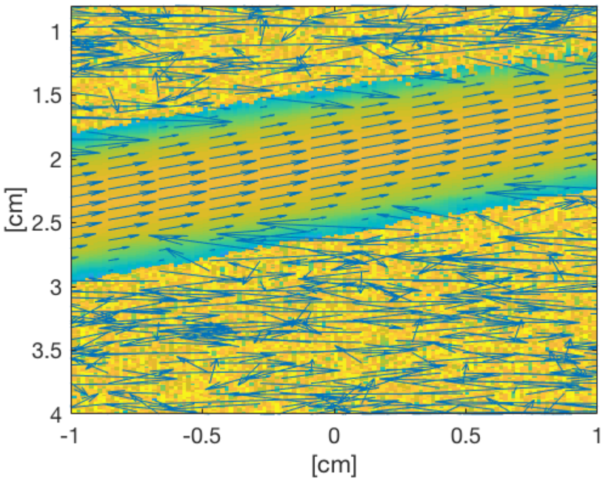

Figure 4.6: Flow from the simulated straight tube phantom, with noise added such that the SNR is 0 dB. The packet size was 150, and aliasing correction was used before vector velocity estimation.

Figure 4.5 and 4.6 indicate that the proposed method is able to correct for aliasing even when the SNR is as low as 0 dB. However, it was difficult to design a mask that masks out the noise outside the vessel, as the noise was as powerful as the signal.

4.2 Phantom experiments

As a packet size of 150 resulted in good performance of the proposed correction method in the simulation study, the same packet size was also used in the phantom experiment. Figure 4.7 shows a visualization of the phantom flow using a Doppler packet size of 150, where the maximum measurable velocity is 1.7 m/s. The underlying B-mode image is the coherent sum of the images from the 11 steering angles. The autocorrelation estimates were used to generate both the color flow image and the overlaid velocity profile.

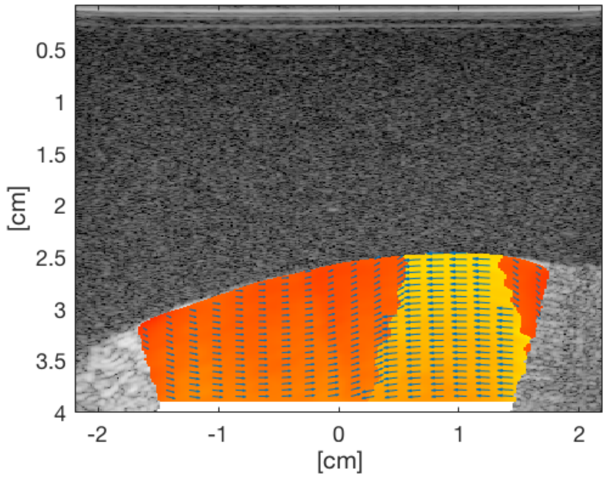

Figure 4.7: Measured velocities in the phantom when a velocity profile of 1.7 m/s was used. The vector velocities overlaid are before aliasing correction. The darker regions in the figure correspond to regions with higher Doppler shifts .

It may be observed that the velocity profile is uniform to a large extent. However, the velocity estimates are divided into three regions with rapid flow changes in the boundaries. In the regions with red color-coding, the velocities estimates are in the wrong direction, due to aliasing.

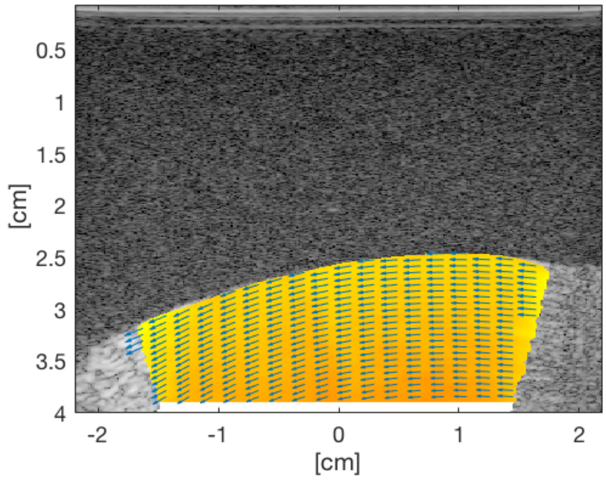

Figure 4.8: Measured velocities in the phantom when a velocity profile of 1.7 m/s was used. The vector velocities overlaid are after the aliasing correction.

The aliasing correction was further applied, with results shown in Figure 4.8. It may be observed that all vector velocities are now similar and all got the same flow conditions. Figure 4.9 shows some intermediate steps in the aliasing correction method, including the autocorrelation phase angles in selected regions.

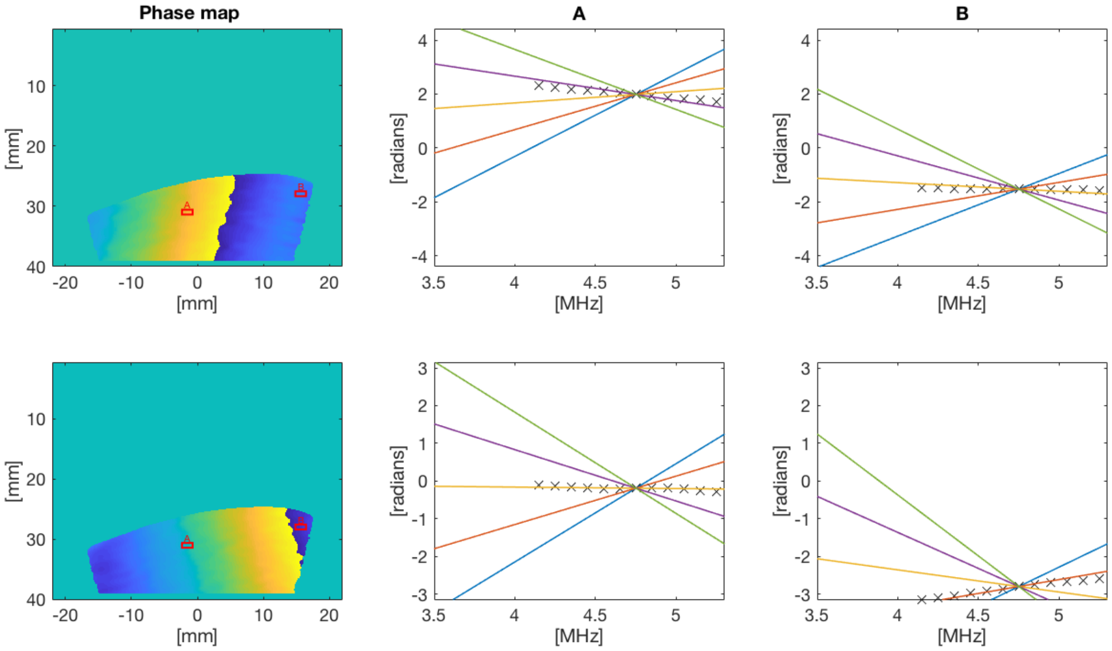

Figure 4.9: Upper panels: a map of the autocorrelation phase angle showing measured phase shift for pixel A with aliasing order -1, and for pixel B with no aliasing. The plots are showing the phase angle of the autocorrelation estimate as a function of fast time filter center frequency. Lower panels: The corresponding figures for angle 2, where pixel A has no aliasing and pixel B has aliasing order 1.

Another velocity profile where the maximum measurable velocity is 2.3 m/s was used to further challenge the method, with results shown in Figure 4.10.

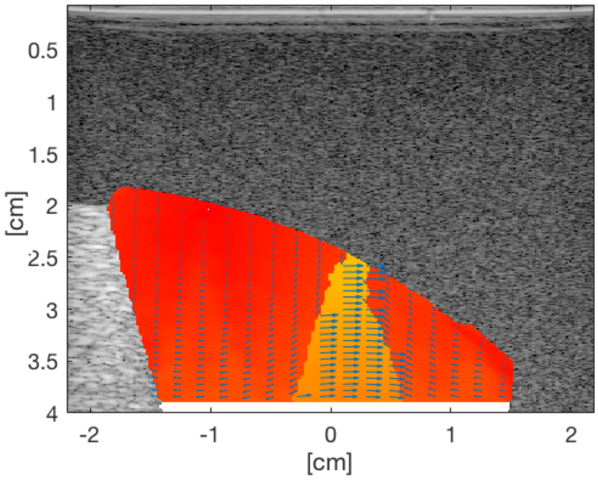

Figure 4.10: Velocity estimates from the spinning phantom with a maximum velocity of 2.3 m/s was used, before aliasing correction. The darker regions in the figure contain aliased velocity estimates.

Note that the contain aliased velocity estimates higher aliasing orders than the previous one, where the velocities has aliasing order 2 for one of the angles. The aliasing correction was used with results shown in Figure 4.11.

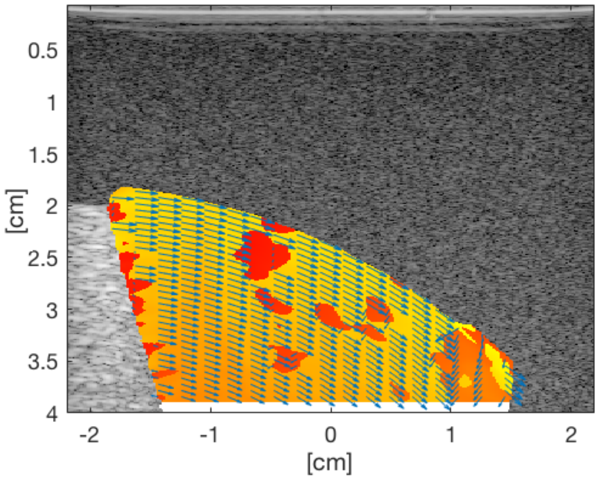

Figure 4.11: Measured velocities in the phantom where a velocity profile of 2.3 m/s was used. The vector velocities overlaid are after the aliasing correction. The darker regions corresponds the dropouts of the aliasing correction method used.

Note that in this recording the probe was held in the upside down, so that velocities are mirrored compared to the previous example. As can be seen in in Figure 4.11, most of the vector velocity estimates are correct, but there are several regions with erroneous aliasing correction.

4.3 In Vivo Imaging

Figure 4.12 illustrates the blood flow in the carotid artery of the healthy volunteer, with acquisitions using Doppler packet sizes of 50 and 150.

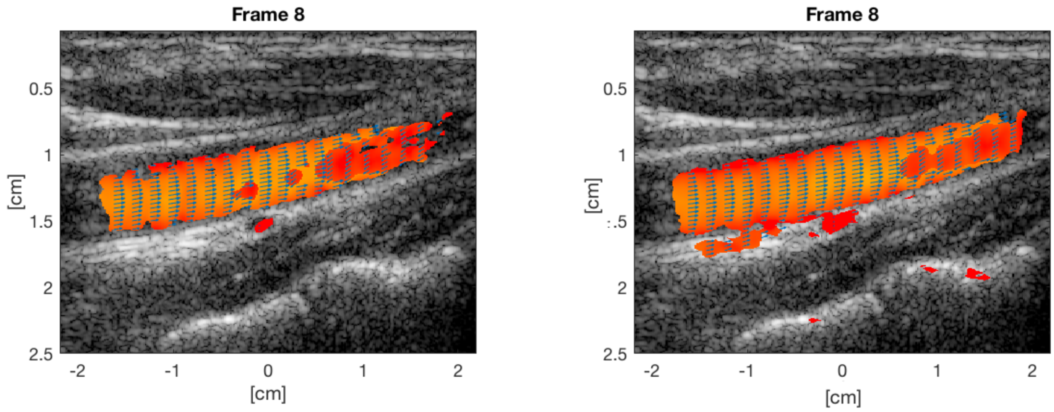

Figure 4.12: Left panel: Blood flow of the healthy volunteer with vector velocities overlaid before aliasing correction. A Doppler packet size of 50 was used in acquisition. Right panel: the corresponding image using a packet size of 150.

The darker regions in both images contain flow in the opposite direction, and are obviously affected by aliasing.

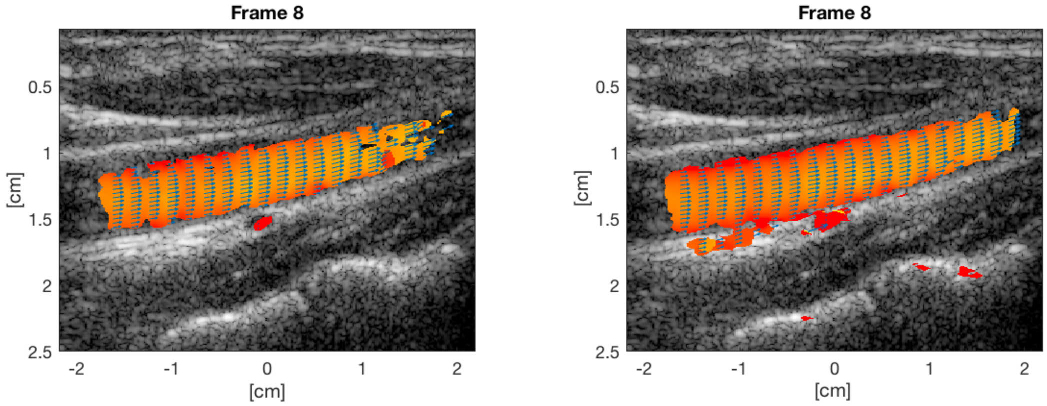

Figure 4.13: Left Panel: Blood flow of healthy volunteer using a packet size of 50. Right panel: corresponding image when using a packet size of 150

Figure 4.13 shows the blood flow from the same frame after correcting for aliasing. Some regions with erroneous aliasing correction can be seen using a packet size of 50. Phase angles as a function of filter center frequency when using a packet size of 150 is displayed in Figure 4.14.

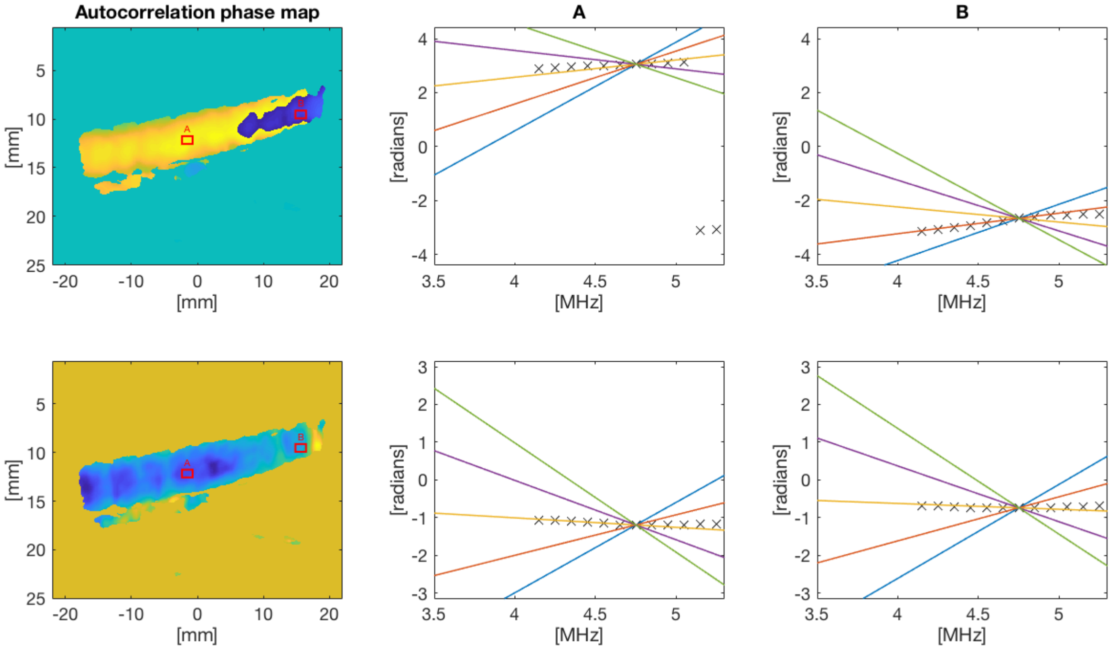

Figure 4.14: Upper panels: a map of the autocorrelation phase angle and the measured phase shifts for pixel A with no aliasing, and for pixel B with aliasing order 1. The plots show the phase angle of the autocorrelation estimate as a function of fast time filter center frequency. Lower panels: The corresponding figures for angle 2, where both pixel A and B have no aliasing.

Another data frame from the same recording, but in systole this time is visualized in Figure 4.15. A packet size of 150 was used in the acquisition.

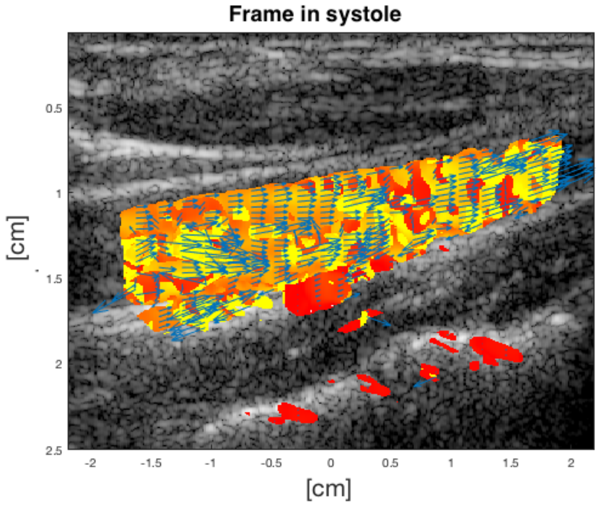

Figure 4.15: Blood flow of the healthy volunteer in systole before aliasing correction.

It is clearly shown here that the systolic contains higher velocities, which corresponds to expectations as the blood flow accelerates in systole. However, large regions with erroneous aliasing correction may be observed in Figure 4.16, when applying the correction method.

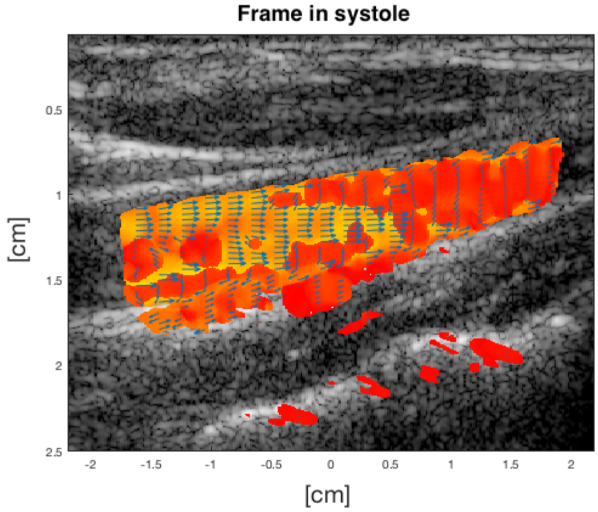

Figure 4.16: Blood flow of the healthy volunteer in systole after aliasing correction.

4.3.1 SNR study

Figure 4.5 shows the blood flow of the healthy volunteer using frame 8 that contains relatively high velocities with some regions affected by aliasing after adding a noise with the same mean power as the blood signal, giving a SNR value of 0.

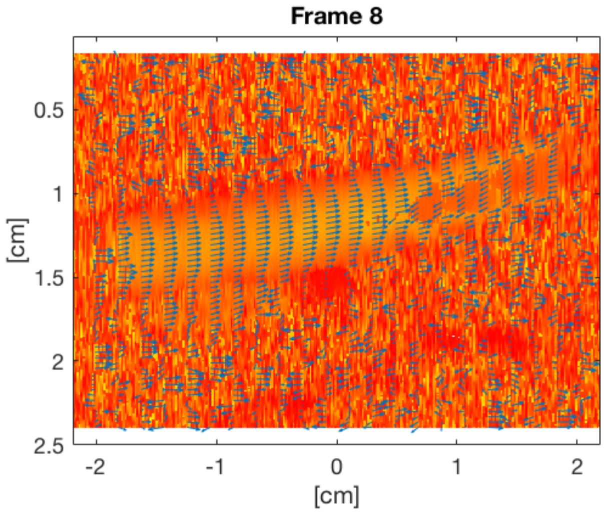

Figure 4.17: Blood flow of the healthy volunteer after adding noise, before the aliasing correction.

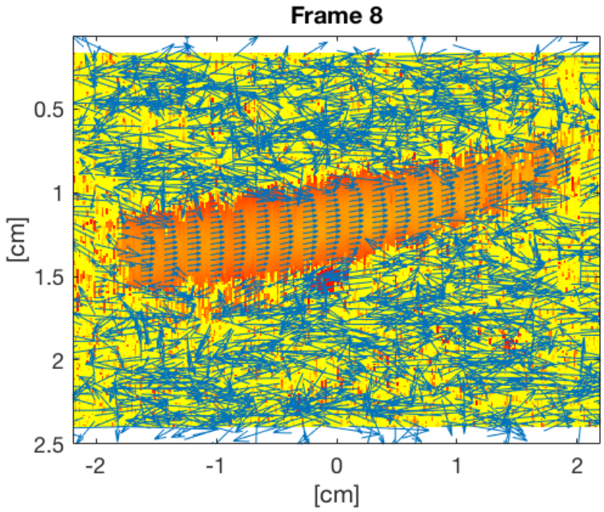

Figure 4.18: Flow from the straight tube with a packet size of 150 with noise added, after the aliasing correction.

Figure 4.18 shows the blood flow from the same frame with noise signal added, after applying the aliasing correction. Figure 4.17 and 4.18 indicate that the method is able to correct for aliasing even when the SNR is as low as 0 dB. As for the simulation study, it was difficult to design a mask that masks out the noise outside the ROI, as the noise was as powerful as the signal.

Chapter 5

Discussion

In this work we have proposed a new method for aliasing correction to improve the robustness of vector Doppler techniques. The method was validated using a simulation study, a phantom experiment and in-vivo recordings from a healthy volunteer.

The results from the simulation study indicate that aliasing errors are largely corrected when applying the proposed aliasing correction method. We used a plane wave setup for the vector Doppler acquisition using Doppler packet sizes of 50, 100 and 150 and the results showed that the performance of the method improves when the Doppler packet size increases. This may be explained due to the fact that variance decreases with increasing packet size, as the autocorrelation estimates are averaged over a larger number of Doppler samples.

The results from the phantom recording show that when using a velocity of 1.7 m/s, the performance of the method is perfect. However, using a velocity of 2.3 m/s gave an aliasing order of 2 for one of the steering angles, and the aliasing correction failed in some of the regions with the highest Doppler shifts. Because both spectral bandwidth of the slow time signal and variance of the autocorrelation method increases with increasing velocities, the phase angle estimates will have high variance when the aliasing order is 2. This is most likely the cause of the regions with erroneous aliasing correction.

It was also shown that the aliasing method can be used *in vivo*, with promising results. The *in vivo* recordings also indicate the same as the simulation results, that higher Doppler packet sizes improved the performance of the method. The results from the *in vivo* recordings in systole (see Figure 4.16), show that the proposed correction method sometimes fails when the flow signal contains very high velocities or accelerated flow.

Although the aliasing correction method does not perform well when we have high variance, the method has shown high robustness for low SNRs. This is observed from the results from simulations and the in vivo ultrasound recordings, where noise with the same power as the signal was added in both cases (see Figures 4.6 and 4.18). However, the noise that was added is not realistic, as real noise will occur before beamforming in practise.

Using relatively high packet sizes as we did in this work will result in a reduction of frame rate. However, the frame rate of 39 frames/s that we got using a Doppler packet size of 150 was arguably high enough for the application. This is mostly because only few firings were used for B-mode. Another important challenge the aliasing correction method might have in practice is that the relatively high packet sizes require more computational power. However fast real-time beamformers with parallel processors might solve this problem.

Future work includes improving the proposed method so it is more robust for higher aliasing orders.

Chapter 6

Conclusion

A duplex acquisition and processing scheme for vector Doppler with aliasing correction has been evaluated in this work, using simulations, phantom experiments and *in vivo* recordings.

The results indicated that the method produces reliable vector velocity estimates for velocities up to three times the Nyquist limit when having a Doppler packet size of 150. The method was also robust to low SNR, being able to correct for aliasing even for SNR values as low as 0 dB. The proposed method failed in some of the regions with aliasing order of 2. Lower robustness of the method was also observed when lower packet sizes of 50 and 100 was used. After further validation, the proposed method may be used in a future duplex setup for real-time vector Doppler imaging with aliasing correction.

Bibliography

[1] World Health Organization,*"Cardiovascular disease."* 2018.

[2] I. K. Ekroll, J. Avdal, A. Swillens, H. Torp, "An Extended Least Squares Method for Aliasing-Resistant Vector Velocity Estimation" *IEEE Transactions on Ultrasonics, Ferroelectrics and Frequency Control.*

[3] I. K. Ekroll, H. Torp and L. Løvstakken, ”In vivo Vector Flow Imaging With Retrospective Pulsed Wave Doppler”,*IEEE International Ultrasonics Symposium Proceedings* 2012

[4] I. K. Ekroll, A. Swillens, P. Segers, T. Dahl, H. Torp and L. Løvstakken, ”Simultaneous quantification of flow and tissue velocities based on multi-angle plane wave imaging”, accepted for publication in *IEEE Transactions on Ultrasonics, Ferroelectrics and Frequency Control.*

[5] "Doppler Ultrasound and Signal Processing Theory." *Ultrasound in Medicine and Biology,* 321-345. 2013

[6] S. Satomura, “Ultrasonic Doppler method for the inspection of cardiac functions1957.

[7] D. Franklin, W. Schlegal, and R. Rushmer, “Blood flow measured by Doppler frequency shift of backscattered ultrasound,” 1961.

[8] I. Edler and H. C.H., “The use of the ultrasonic reflectoscope for the continuous recording of movements of heart walls,” Kungl fysiogr s¨allsk 1954.

[9] Y. B. Ahn and S. B. Park, "Estimation of mean frequency and variance of ultrasonic Doppler signal by using second-order autoregressive model."*IEEE Transactions on Ultrasonics, Ferroelectrics and Frequency Control.*1991

[10] B. Delannoy, R. Torguet, C. Bruneel, E. Bridoux, J. M. Rouvaen, and H. Lasota, “Acoustical image reconstruction in parallel processing analog electronic systems,”*Journal of Applied Physics,* 1979.

[11] J. Udesen, F. Gran, K. Hansen, J. Jensen, C. Thomsen, and M. Nielsen, “High Frame-Rate Blood Vector Velocity Imaging Using Plane Waves: Simulations and Preliminary Experiments,*IEEE Transactions on Ultrasonics, Ferroelectrics and Frequency Control.*2008

[12] S. Nikolov and J. Jensen, “In-vivo synthetic aperture flow imaging in medical ultrasound,” *IEEE Transactions on Ultrasonics, Ferroelectrics and Frequency Control.*2003

[13] G. Montaldo, M. Tanter, J. Bercoff, N. Benech, and M. Fink,“Coherent plane-wave compounding for very high frame rate ultrasonography and transient elastography,” *Ultrasonics, Ferroelectrics and Frequency Control, IEEE Transactions on,*vol. 56, pp. 489 –5062009

[14] K. Ferrara and G. Deangelis, "Color flow mapping". 1997

[15] W. H. Berwer and K. A. Kraft, "Angle independent Doppler color imaging: Determination of accuracy and a method of display." *Ultrasound in Medicine and Biology,*145-155. 1994.

[16] H. Torp, K. Kristoffersen and B. Angelsen, "On the joint probability density function for the autocorrelation estimates in ultrasound color flow imaging."*IEEE Transactions on Ultrasonics, Ferroelectrics and Frequency Control.*1995

[17] H. Tor, K. Kristoffersen and B. Angelsen, "Autocorrelation technique in color flow imaging, signal model and statistical properties of the autocorrelation estimates." *IEEE Transactions on Ultrasonics, Ferroelectrics and Frequency Control.*1994

[18] M. E. Anderson and G. E. Trahey, "A seminar on k -space applied to medical ultrasound." *Department of Biomedical Engineering, Duke University.* 2000

[19] I. K. Ekroll, H. Torp and L. Løvstakken, ”Spectral Doppler Estimation Utilizing 2D Spatial Information and Adaptive Signal Processing”,*IEEE Transactions on Ultrasonics, Ferroelectrics and Frequency Control.*

[20] T. L. Szabo, *"Diagnostic ultrasound imaging : inside out",* Amsterdam ; Boston, Elsevier Academic Press. 2004.

[21] M. Spencer and J. Reid, “Quantitation of carotid stenosis with continuous-wave (C-W) Doppler ultrasound,”*Stroke*1979.

[22] G.-M. von Reutern, “Measuring the degree of internal carotid artery stenosis,”*Perspectives in Medicine,*2012.

[23] H. Torp, "Clutter Rejection Filters in Color Flow Imaging: A theoretical approach." *IEEE Transactions on Ultrasonics, Ferroelectrics and Frequency Control.* 1997.

[24] I. K. Ekroll, A. Swillens, P. Segers, H. Torp and L. Løvstakken, ”Simultaneous quantification of flow and tissue velocities based on multi-angle plane wave imaging with extended velocity range”, *IEEE International Ultrasonics Symposium Proceedings.* 2011.

[25] B. Angelsen and H. Torp, "Principles of medical ultrasound imaging and measurements." *Ultrasound Imaging* 2000.

[26] M. Fox, “Multiple crossed-beam ultrasound doppler velocimetry,” *Sonics and Ultrasonics, IEEE Transactions on*, vol. 25, pp. 281 –286, sept. 1978.

[27] J. Flynn, R. Daigle, L. Pflugrath, K. Linkhart and P. Kaczkowski, “Estimation and display for vector Doppler imaging using planewave transmissions,” in *Proc. IEEE Ultrason. Symp.*, 2011

[28] T.D.Fredriksen and H.Torp, "Basic Ultrasound and Signal Processing Theory." 2013.

[29] *Introduction to IQ demodulation of RF-data.* Trondheim: IFBT, NTNU. 1999.

[30] G. E. Trahey, J. W. Allison, and O. T. von Ramm, “Angle independent ultrasonic detection of blood flow,*Biomedical Engineering, IEEE Transactions* 1987.

[31] P. J. Frinking, A. Bouakaz, J. Kirkhorn, F. J. Cate and N. D. Jong, "Ultrasound Contrast Imaging: Current and New Potential Methods." *Ultrasound in Med. and Biol.* 2000.

[32] P. Vaitkus and R. Cobbold, “A comparative study and assessment of Doppler ultrasound spectral estimation techniques part I: Estimation methods,”*Ultrasound in medicine biology.*1988.

[33] J. Jensen, “Field: A program for simulating ultrasound systems,” *Med.Biol.Eng.Comput.* 1996.

[34] I. Ekroll, H. Torp, and L. Lovstakken, “Spectral Doppler Estimation Utilizing 2D Spatial Information and Adaptive Signal Processing,”*IEEE transactions on ultrasonics, ferroelectrics, and frequency control.*